



THE UNIVERSITY *of* EDINBURGH

Edinburgh Research Explorer

## Ultrahigh-current-density niobium disulfide catalysts for hydrogen evolution

### Citation for published version:

Yang, J, Mohmad, AR, Wang, Y, Fullon, R, Song, X, Zhao, F, Bozkurt, I, Augustin, M, Santos, EJG, Shin, HS, Zhang, W, Voiry, D, Jeong, HY & Chhowalla, M 2019, 'Ultrahigh-current-density niobium disulfide catalysts for hydrogen evolution', *Nature Materials*, vol. 18, no. 12, pp. 1309-1314.  
<https://doi.org/10.1038/s41563-019-0463-8>

### Digital Object Identifier (DOI):

[10.1038/s41563-019-0463-8](https://doi.org/10.1038/s41563-019-0463-8)

### Link:

[Link to publication record in Edinburgh Research Explorer](#)

### Document Version:

Peer reviewed version

### Published In:

Nature Materials

### General rights

Copyright for the publications made accessible via the Edinburgh Research Explorer is retained by the author(s) and / or other copyright owners and it is a condition of accessing these publications that users recognise and abide by the legal requirements associated with these rights.

### Take down policy

The University of Edinburgh has made every reasonable effort to ensure that Edinburgh Research Explorer content complies with UK legislation. If you believe that the public display of this file breaches copyright please contact [openaccess@ed.ac.uk](mailto:openaccess@ed.ac.uk) providing details, and we will remove access to the work immediately and investigate your claim.



## Ultrahigh current density niobium disulfide catalysts for hydrogen evolution

Jeun Yang<sup>1, †</sup>, Abdul Rahman Mohamad<sup>2, †</sup>, Yan Wang<sup>1</sup>, Raymond Fullon<sup>1</sup>, Xiuju Song<sup>1,3</sup>, Fang Zhao<sup>4</sup>, Ibrahim Bozkurt<sup>1</sup>, Mathias Augustin<sup>5</sup>, Elton J. G. Santos<sup>5\*</sup>, Hyeon Suk Shin<sup>6</sup>, Damien Voiry<sup>7</sup>, Hu Young Jeong<sup>8,\*</sup>, Manish Chhowalla<sup>1,3\*</sup>

### Affiliations:

<sup>1</sup>*Materials Science and Engineering, Rutgers University, 607 Taylor Road, Piscataway, New Jersey 08854, USA.*

<sup>2</sup>*Institute of Microengineering and Nanoelectronics, National University of Malaysia (UKM), 43600 Bangi, Selangor, Malaysia*

<sup>3</sup>*SZU-RUT Collaborative Innovation Center for Optoelectronic Science & Technology, International Collaborative Laboratory of 2D Materials for Optoelectronics Science and Technology of Ministry of Education, College of Optoelectronic Engineering, Shenzhen University, Shenzhen 518060, China.*

<sup>4</sup>*Department of Physics, Princeton University, Jadwin Hall, Princeton New Jersey 08544, USA*

<sup>5</sup>*School of Mathematics and Physics, Queen's University Belfast, BT71NN, United Kingdom*

<sup>6</sup>*Department of Chemistry and Department of Energy Engineering, Low-Dimensional Carbon Materials Center, Ulsan National Institute of Science and Technology (UNIST), UNIST-gil 50, Ulsan 44919, Republic of Korea*

<sup>7</sup>*Institut Européen des Membranes (I.E.M.), University of Montpellier, Place Eugène Bataillon, 34095 Montpellier, France*

<sup>8</sup>*UNIST Central Research Facilities (UCRF) and School of Materials Science and Engineering, UNIST, Ulsan 689-798, Republic of Korea*

\*Correspondence to: [e.santos@qub.ac.uk](mailto:e.santos@qub.ac.uk), [hulex@unist.ac.kr](mailto:hulex@unist.ac.kr) and [manish1@soe.rutgers.edu](mailto:manish1@soe.rutgers.edu)

<sup>†</sup> *These authors contributed equally to this work.*

Two-dimensional metallic transition metal dichalcogenides (2D TMDs) such as 1T phases of MoS<sub>2</sub><sup>1,2</sup> and WS<sub>2</sub><sup>3</sup>, NbS<sub>2</sub><sup>4</sup>, TaS<sub>2</sub><sup>4-6</sup> and VS<sub>2</sub><sup>7,8</sup> have been studied as potentially inexpensive and earth abundant electrocatalysts for the hydrogen evolution reaction (HER). The performance of HER catalysts is typically evaluated in terms of overpotential at which the reaction starts and the Tafel slope – a measure of the over-potential required to increase a reaction by a factor of 10. The overpotential and Tafel slope values of metallic phases and edges<sup>9</sup> of 2D TMDs approach those of Pt nanoparticles – the best HER catalyst. However, despite substantial progress the overall current density of 2D TMD catalysts remains orders of magnitude lower ( $\sim 10 - 100 \text{ mA-cm}^{-2}$ ) than industrial Pt and Ir electrolyzers ( $> 1,000 \text{ mA-cm}^{-2}$ )<sup>10,11</sup>. Here, we report the synthesis of metal intercalated metallic 2H phase of niobium disulfide (Nb<sub>1+x</sub>S<sub>2</sub> where  $x$  is  $\sim 0.35$ )<sup>12</sup> as a HER catalyst that is capable of evolving hydrogen at current densities of  $> 5,000 \text{ mA-cm}^{-2}$  at an overpotential of  $\sim 420 \text{ mV}$  versus reversible hydrogen electrode (RHE). We find the exchange current density at 0 V for 2H Nb<sub>1.35</sub>S<sub>2</sub> catalysts to be  $\sim 0.8 \text{ mA-cm}^{-2}$  (comparable to that of noble metals), corresponding to a turnover frequency of  $\sim 0.2 \text{ s}^{-1}$ . We demonstrate a proof of concept electrolyzer based on 2H Nb<sub>1.35</sub>S<sub>2</sub> cathode that is capable of generating current densities of  $1000 \text{ mA-cm}^{-2}$ . Our theoretical results reveal that the 2H phase Nb<sub>1.35</sub>S<sub>2</sub> with Nb terminated surface has free energy for hydrogen adsorption that is close to thermoneutral, facilitating HER. The 2H phase Nb<sub>1+x</sub>S<sub>2</sub> could therefore be a viable non-precious metal catalyst for practical electrolyzers used to generate hydrogen.

Ultra-thin layers of TMD catalysts exhibit improved electrocatalytic performance due to efficient charge injection and transfer to active sites<sup>13,14</sup>. Increasing the conductivity via engineering of metallic phases<sup>2,15,16</sup> and edges<sup>14,17-19</sup> also leads to substantial improvement in catalytic properties. To this end, metallic 1T phase of semiconducting MoS<sub>2</sub> induced by lithium chemistry<sup>1,2,20</sup> has been widely studied for HER catalysis. Recently, multi-layers of thin metallic TMDs such as NbS<sub>2</sub><sup>4</sup>, TaS<sub>2</sub><sup>5</sup>, and VS<sub>2</sub><sup>7</sup> have also been studied for HER. The key advantage of metallic TMDs according to theory is that the entire basal plane is catalytically active for the HER<sup>4,21,22</sup>, unlike in semiconducting MoS<sub>2</sub> where only the metallic edges are active<sup>9</sup>. However, in contrast with noble metal catalysts such as Pt nanoparticles, the electronic structure of atomically thin materials is strongly influenced by local electrochemical reactions. For example, in the case of metallic 1T

phase MoS<sub>2</sub>, the adsorption of protons on the surface – the first step in the HER – can dramatically reduce the conductivity of the 2D nanosheets<sup>21</sup>, which can slow down the reaction kinetics and reduce the overall current density. Thus, a fine balance must be achieved between reducing the thickness of catalysts and maintaining metallic nature of 2D materials to maximize catalytic performance.

NbS<sub>2</sub> is a layered material that can exist in the hexagonal (2H phase) or rhombohedral (3R) crystal configurations (see Extended Data Fig. 1a,b,d,e). Metallic 2H phase NbS<sub>2</sub> has been predicted to be one of the most efficient electrocatalysts for the HER among the different types of TMDs<sup>22</sup>. In addition to the 2H and 3R phases, an unexplored non-layered polytype with Nb<sub>1+x</sub>S<sub>2</sub> (where  $x$  is  $\sim 0.35$ ) stoichiometry, first synthesized in 1960 (Ref<sup>12</sup>), consisting of excess niobium intercalated between NbS<sub>2</sub> layers is also stable (see Extended Data Fig. 1c,f). We find that the intercalated Nb<sub>1+x</sub>S<sub>2</sub> phase can be synthesized by adjusting the CVD growth parameters (see Methods). Atomic force microscopy (AFM) image of typical Nb<sub>1+x</sub>S<sub>2</sub> crystals synthesized by chemical vapor deposition is shown in Figure 1a. Films of varying thicknesses ranging from 2 nm to 50 nm with lateral dimensions of  $\sim 0.5 - 1 \mu\text{m}$  were realized by CVD on substrates such as SiO<sub>2</sub> and glassy carbon. We find that the phase of NbS<sub>2</sub> is dependent on the thickness of the material (Extended Data Fig. 2a-c). The electron diffraction patterns corresponding to the phases as a function of thickness are provided in Extended Data Fig. 2d,e. In particular, 2H – Nb<sub>1+x</sub>S<sub>2</sub> is predominantly observed in crystals with thickness of less than  $\sim 20$  nm while the 3R phase is primarily stable for thicker samples. High-resolution annular dark field (ADF) cross-sectional STEM images of Nb<sub>1+x</sub>S<sub>2</sub> clearly reveal Nb intercalation in both 2H phase (Figure 1b) and the 3R phase (Figure 1c). The  $d_{(0002)}$  spacing for the 2H intercalated phase ( $6.35 \text{ \AA}$ ,  $c = 12.60 \text{ \AA}$ ) was found to be close to the theoretical value of the Nb<sub>1.35</sub>S<sub>2</sub> composition. The lower contrast in ADF image of the intercalated Nb planes is attributed to partial occupation of these sites (occupancy of 0.35 in excess layers versus 1 in the NbS<sub>2</sub> 2H and 3R layers). Additional evidence for intercalated Nb atoms in the form of  $Z$  contrast scans of atoms and chemical analyses are provided in Extended Data Fig. 3a,b. Direct synthesis of intercalated layered compounds with CVD is highly beneficial for preserving the high quality of the material. That is, intercalation involving wet chemistry can lead to undesirable local reactions and deterioration of the material properties.

The catalytic properties of NbS<sub>2</sub> and other metallic TMDs such as TaS<sub>2</sub> and VS<sub>2</sub> have been measured in several studies<sup>4,5,7</sup>. The results generally reveal Tafel slopes of  $\sim 40$  mV-dec<sup>-1</sup> and low overpotential values of tens of millivolts vs RHE. For comparison, the overpotential at which HER proceeds for Pt nanoparticles is 0 V vs RHE with a corresponding Tafel slope of  $\sim 30$  mV-dec<sup>-1</sup>. Despite the promising overpotentials and Tafel slopes achieved with metallic TMD catalysts, the maximum reported current density value has remained around  $\sim 100$  mA-cm<sup>-2</sup>. The current density is limited by the multiple layers of metallic TMDs. That is, in contrast to phase transformed 1T metallic MoS<sub>2</sub> nanosheets that are single layered, it is generally challenging to synthesize or exfoliate metal TMDs down to the monolayer. Thus, most metallic NbS<sub>2</sub> and TaS<sub>2</sub> catalysts are multilayered and therefore electrons injected from the glassy carbon support must overcome the van der Waals gaps between the layers to reach the active sites on the surface. This increases the charge transfer resistance and thus the catalytic activity has been demonstrated to be inversely related to the number of layers in TMDs<sup>23</sup>. In the case of single layers, while the charge transfer kinetics are improved, the current carrying capability is lower and therefore the overall current density that can be achieved is also lower. Furthermore, the recombination of protons with free electrons on the surface of the single layer catalysts (the first step of the reaction) decreases the concentration of free carriers and therefore the conductivity<sup>21</sup>, reducing the kinetics of the HER and lowering the current density.

We have tested the catalytic performance of metallic 2H Nb<sub>1.35</sub>S<sub>2</sub> with improved conductivity via elimination of van der Waals gaps between layers. This Nb<sub>1.35</sub>S<sub>2</sub> phase for HER was directly grown at 1273 K (CVD parameters are described in Methods) on high-quality glassy carbon electrodes. The HER was measured in 0.5M H<sub>2</sub>SO<sub>4</sub> electrolyte (see Methods for detailed description of measurements). The current density as a function of potential (vs RHE) from 2H, 3R NbS<sub>2</sub>, and intercalated 2H phase Nb<sub>1.35</sub>S<sub>2</sub> along with those from 3R Nb<sub>1.35</sub>S<sub>2</sub>, 2H and 1T phases of MoS<sub>2</sub> and WS<sub>2</sub> ref<sup>3</sup>, 2H and 3R NbS<sub>2</sub>, and Pt for comparison are shown in Figure 2a. It can be clearly seen from the polarization curves that the current density for the 2H Nb<sub>1.35</sub>S<sub>2</sub> is exceptionally large, reaching 1000 mA-cm<sup>-2</sup> at  $\sim 370$  mV and 5,000 mA-cm<sup>-2</sup> at  $\sim 420$  mV. This current density is obtained from careful analyses of the catalytic active area. We have examined of numerous scanning electron microscope images to determine the areal coverage of catalyst material on the glassy carbon surface. We found that  $20\% \pm 5\%$  of the electrode surface is covered by the catalyst

particles, see Extended Data Fig. 4. In addition to the areal coverage, we also carefully measured the electrochemical surface area (see Extended Data Fig. 5) to find the roughness factor ( $RF = 11 \pm 3$ ). Using this value, we were able to accurately determine the active area of the catalyst and use it to calculate the current density. It can be seen from Figure 2b, which provides an expanded view of the low overpotential region in Figure 2a, that the cathodic potential at which the HER starts is less than 100 mV (overpotential of  $< 150$  mV) for the 2H  $Nb_{1.35}S_2$  catalysts. The reaction for metallic 2H  $Nb_{1.35}S_2$  phase starts immediately upon application of the potential and proceeds slowly initially but as the potential is increased, it proceeds rapidly with very high current densities. The Tafel slopes shown in Figure 2c provide additional information about the rate limiting step in the catalytic performance. Tafel slope values can vary from  $30 \text{ mV-dec}^{-1}$  for Pt –indicating that HER is limited by the recombination of adsorbed hydrogens – to  $> 120 \text{ mV-dec}^{-1}$  where adsorption of protons limits the catalytic activity. It can be seen that the Tafel slope for 2H phase  $Nb_{1.35}S_2$  catalysts is  $43 \text{ mV-dec}^{-1}$  (and  $\sim 38 \text{ mV-dec}^{-1}$  after  $iR$  correction) at low overpotentials (100 – 120 mV), which is comparable to what has been measured for metallic 1T phase  $MoS_2$  and  $NbS_2$  and suggests that the rate limiting reaction is the desorption of hydrogens. At higher potentials (120 – 250 mV), the Tafel slope increases to  $\sim 70 \text{ mV-dec}^{-1}$  (or  $65 \text{ mV-dec}^{-1}$  after  $iR$  correction), suggesting that hydrogen adsorption or diffusion of protons to active sites limits the reaction. To differentiate between these two mechanisms, we made HER measurements under agitation to increase diffusion of protons and found that the results are largely unchanged. These observations are consistent with theoretical results that show that, unlike Pt, metallic TMD catalysts such as  $NbS_2$  possess dilute adsorption of hydrogens on the surface at low potentials but the high activity per site is retained at higher potentials where coverage of adsorbed hydrogens increases<sup>4</sup>. In addition to the overpotential and Tafel slope, we have also measured the number of hydrogen molecules evolved per second (the turnover frequency, TOF) for the catalysts. We have found that the TOF for the 2H phase  $Nb_{1.35}S_2$  catalysts to be in excess of  $100 \text{ s}^{-1}$  at 280 mV. The TOF from this work compares favorably with other reports, as summarized in Figure 2d. The exchange current density at 0 V for the  $Nb_{1.35}S_2$  phase catalysts was found to be  $\sim 0.8 \text{ mA-cm}^{-2}$  which corresponds to a TOF of  $0.17 \text{ s}^{-1}$ . For comparison, the exchange current density for Pt (111) is  $0.5 - 1 \text{ mA-cm}^{-2}$  corresponding to TOF of  $\sim 1 \text{ s}^{-1}$  (Ref<sup>9</sup>) and for metallic 2D TMDs the values are  $0.02 \text{ mA-cm}^{-2}$  and  $0.043 \text{ s}^{-1}$  (Ref<sup>3</sup>), suggesting that the turnover for hydrogen evolution is high for 2H phase  $Nb_{1.35}S_2$  catalysts. Summary of the obtained values is provided in Extended Data Table 1.

Impedance measurements on 2H and 3R Nb<sub>1.35</sub>S<sub>2</sub> are shown in Figure 3a. It can be seen that the series resistance for the 2H phase Nb<sub>1.35</sub>S<sub>2</sub> obtained at 1MHz where the phase angle is close to zero is 3.5 Ω due to its high electrical conductivity and indicating good contact with glassy carbon electrode. The charge transfer resistance is 7.4 Ω, facilitating charge injection and transport to active sites. In contrast, the 3R Nb<sub>1.35</sub>S<sub>2</sub> shows higher resistances and diffusion limited activity. This is in agreement with our observations that the 3R phase is less conducting and is stable at higher film thicknesses. Finally, we have measured the electrochemical stability of the electrodes by carrying out over 10000 cycles. The high current density shows remarkable stability with negligible difference in polarization curves and overpotential values after 10,000 cycles (Figure 3b). The above experimental results suggest that intercalation of Nb between 2H phase NbS<sub>2</sub> layers to realize Nb<sub>1.35</sub>S<sub>2</sub> allow realization of practical current densities of > 5,000 mA-cm<sup>-2</sup> – making them potentially useful alternatives to Pt and Ir. To translate the high current densities of 2H phase Nb<sub>1.35</sub>S<sub>2</sub> catalysts into practical device, we fabricated a proof of concept two electrode electrolyzer for water splitting. The device shown in Figure 3c consists of 2H Nb<sub>1.35</sub>S<sub>2</sub> on glassy carbon cathode and a commercial Pt anode. The measurements were carried out at room temperature in 0.5 M H<sub>2</sub>SO<sub>4</sub>. The device characteristics are plotted in Figure 3d, which show that the reaction for the 2H Nb<sub>1.35</sub>S<sub>2</sub> starts around 1.3 V and the current densities reach 1000 mA-cm<sup>-2</sup> at 2.0 V. Proof of concept electrolyzers of this type typically report current densities of 10 – 100 mA-cm<sup>-2</sup> at similar potential values <sup>24</sup>.

To elucidate the fundamental mechanisms responsible for the catalytic performance of 2H Nb<sub>1.35</sub>S<sub>2</sub>, we calculated the thermodynamics of the limiting reaction – the adsorption of hydrogen on the catalyst surface using density functional theory (DFT) including van der Waals interactions. It is well known that the best HER catalysts possess Δ*G* ~ 0 (that is, thermoneutral condition) so that there is a driving force for hydrogen adsorption on the active site but the binding energy is low to allow efficient hydrogen evolution. The results of the calculations are shown in Figure 4. Our theoretical results suggest that both the Nb and S terminations are stable for the Nb<sub>1.35</sub>S<sub>2</sub> phases. We have observed intercalated Nb terminated surface by STEM imaging (see Extended Data Fig. 3c). It can be seen in Figure 4a that the free energy for hydrogen adsorption for the 2H Nb<sub>1.35</sub>S<sub>2</sub> is close to being thermoneutral (~ 0.11 eV) when the surface is terminated by Nb under

0.25 monolayer coverage (Figure 4b). In contrast, the free energy of adsorbed hydrogen is  $\sim 1\text{eV}$  when the surface is terminated by sulfur in  $2\text{H Nb}_{1.35}\text{S}_2$ . The calculations also reveal that the reaction is localized to the surface of the catalysts, as indicated by the charge density diagrams in Figure 4c. The better HER properties of the  $2\text{H Nb}_{1.35}\text{S}_2$  relative to the  $3\text{R Nb}_{1.35}\text{S}_2$  is consistent with the higher density of states at the Fermi level (Figure 4e,f), which translates into higher measured conductivity and better charge transfer kinetics. Thus, our work provides new insight into materials design for achieving high current densities with non-precious metal catalysts.



## Figure captions

**Figure 1 | Images of  $\text{Nb}_{1+x}\text{S}_2$  crystals and atomic structure.** **a**, Atomic force microscopy image of a grown  $\text{Nb}_{1+x}\text{S}_2$  ( $x \sim 0.35$ ) crystals on high quality glassy carbon (scale bar = 1  $\mu\text{m}$ ). **b**, Cross-sectional ADF STEM image of 2H phase  $\text{Nb}_{1.35}\text{S}_2$  and 3R phase  $\text{Nb}_{1+x}\text{S}_2$ , **c**. The dashed white rectangle represents the unit cell of the structure and the corresponding ball and stick model of the unit cell is shown on the right. The red dashed rectangles in the STEM image and the schematic indicate the positions of the intercalated Nb. Since these sites are partially occupied, the contrast of these planes is lower than of the fully occupied Nb sites. The arrows correlate the locations of the atoms in the STEM image with the atoms in the unit cell. The dark green arrows and spheres in the schematic indicate fully occupied Nb sites and light green arrows and spheres in unit cell indicate partially occupied Nb atoms. Z. A. refers to zone axis of the crystal structure. Scale bar = 5  $\text{\AA}$ .

**Figure 2 | HER catalytic activities of different TMDs.** **a**, Polarization curves for 2H-MoS<sub>2</sub>, 1T-MoS<sub>2</sub> and WS<sub>2</sub>, 2H-Nb<sub>1.35</sub>S<sub>2</sub>, 3R-Nb<sub>1.35</sub>S<sub>2</sub>, 2H-NbS<sub>2</sub> and 3R NbS<sub>2</sub> and Pt measured in 0.5M H<sub>2</sub>SO<sub>4</sub> with a scan rate of 5 mVs<sup>-1</sup>. **b**, Expanded view of the low overpotential region in **a**. The reaction starts immediately upon application of voltage, indicating that the onset potential of 2H-Nb<sub>1.35</sub>S<sub>2</sub> is < 100 mV and overpotential is 150 mV. **c**, Tafel slopes of different catalysts obtained from polarization curves in **a**. 2H-Nb<sub>1.35</sub>S<sub>2</sub> shows slope of 43 mV-dec<sup>-1</sup> (38 mV-dec<sup>-1</sup> after *iR* correction) at low overpotentials (100-130 mV, green) and 70 mV-dec<sup>-1</sup> (65 mV-dec<sup>-1</sup> after *iR* correction) at high overpotentials (130-200 mV, red). **d**, TOF values of the 2H-Nb<sub>1.35</sub>S<sub>2</sub> (black line) and other MoS<sub>2</sub>-based catalysts reported in the literature<sup>25,26</sup>. MoS<sub>2</sub> basal planes with sulfur vacancies (blue)<sup>27</sup>, strained MoS<sub>2</sub> basal planes with sulfur vacancies (green)<sup>27</sup> and MoS<sub>2</sub> with low charge transfer resistance,  $R_c$  (magenta)<sup>15</sup>.

**Figure 3 | Electrochemical impedance spectroscopy (EIS), electrochemical stability of Nb<sub>1.35</sub>S<sub>2</sub> and proof of concept electrolyzer demonstration.** **a**, Nyquist plots of 2H phase (red curve) and 3R phase Nb<sub>1.35</sub>S<sub>2</sub>. Magnification of 2H-Nb<sub>1.35</sub>S<sub>2</sub> plot is shown in the inset. The plots (dash line) were fitted using an equivalent circuit to extract the series and charge transfer resistances. **b**, Polarization curves of 2H-Nb<sub>1.35</sub>S<sub>2</sub> before (black curve) and after (red curve) 10,000 cycles. The insets show the percentage of change in overpotential. The error bars are obtained from

at least five measurements. **c**, Photograph of the two electrode electrolyzer device consisting of commercial Pt anode and 2H-Nb<sub>1.35</sub>S<sub>2</sub> cathode. **d**, Polarization curves of water electrolysis showing current density of 1000 mA-cm<sup>-2</sup>.

**Figure 4 | Thermodynamic stability and free-energy calculations for hydrogen evolution for**

**2H-Nb<sub>1.35</sub>S<sub>2</sub> and 3R-Nb<sub>1.35</sub>S<sub>2</sub> phases.** **a**, The free-energy diagram for hydrogen evolution at standard conditions (1 bar of H<sub>2</sub> and pH=0 at 300 K). The energies of the intermediate states are calculated using BEEF-vdW functional as described in the Methods. A coverage of 0.25 ML was used for all calculations. **b**, Optimized geometries for S- and Nb-terminated surfaces of 2H-Nb<sub>1.35</sub>S<sub>2</sub> and 3R-Nb<sub>1.35</sub>S<sub>2</sub> phases. **c**, Charge density difference for H adsorbed on top of Nb-terminated 2H- and 3R-Nb<sub>1.35</sub>S<sub>2</sub> phases. Most of the charge is localized on the surface, with clear differences between 2H- and 3R-Nb<sub>1.35</sub>S<sub>2</sub> phases with the former having larger magnitudes. **e-f**, Density of states (DOS) per atom for Nb-terminated 2H- and 3R-Nb<sub>1.35</sub>S<sub>2</sub> phases projected on different Nb sites. Surface Nb, inner Nb and deep bulk Nb atoms are shown in red, blue and orange, respectively. For a better contrast between the different Nb's atoms, the DOS of surface Nb atoms is highlighted with a filled faint red. Fermi level is set to 0 eV.

Figure 1:

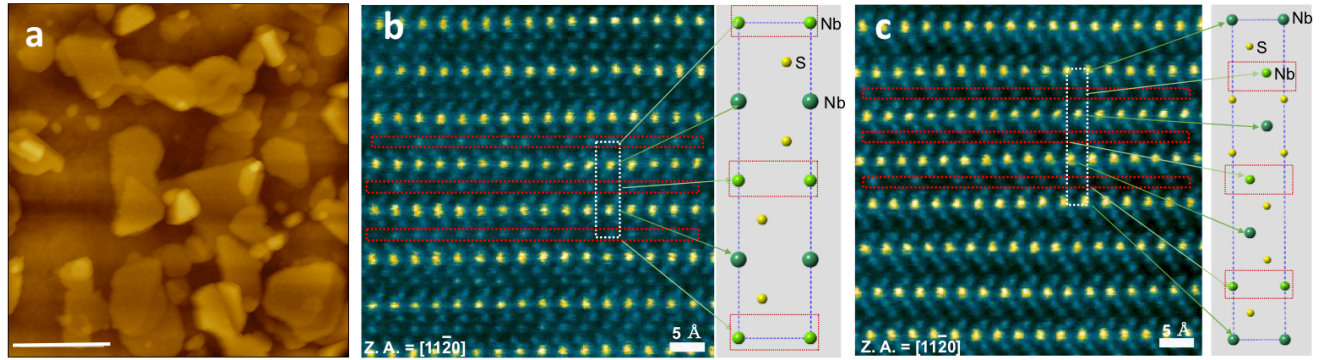


**Figure 2**

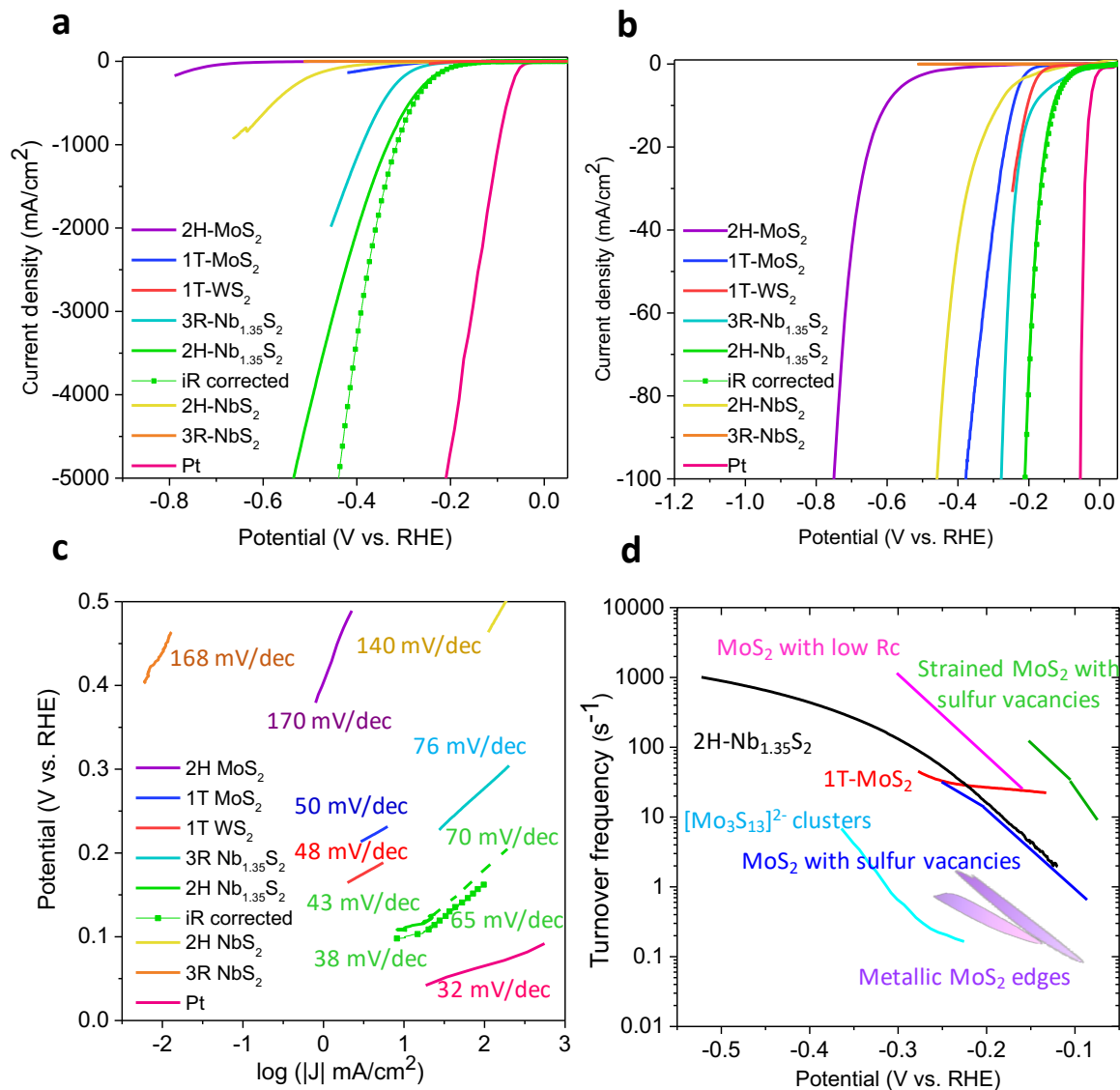


Figure 3

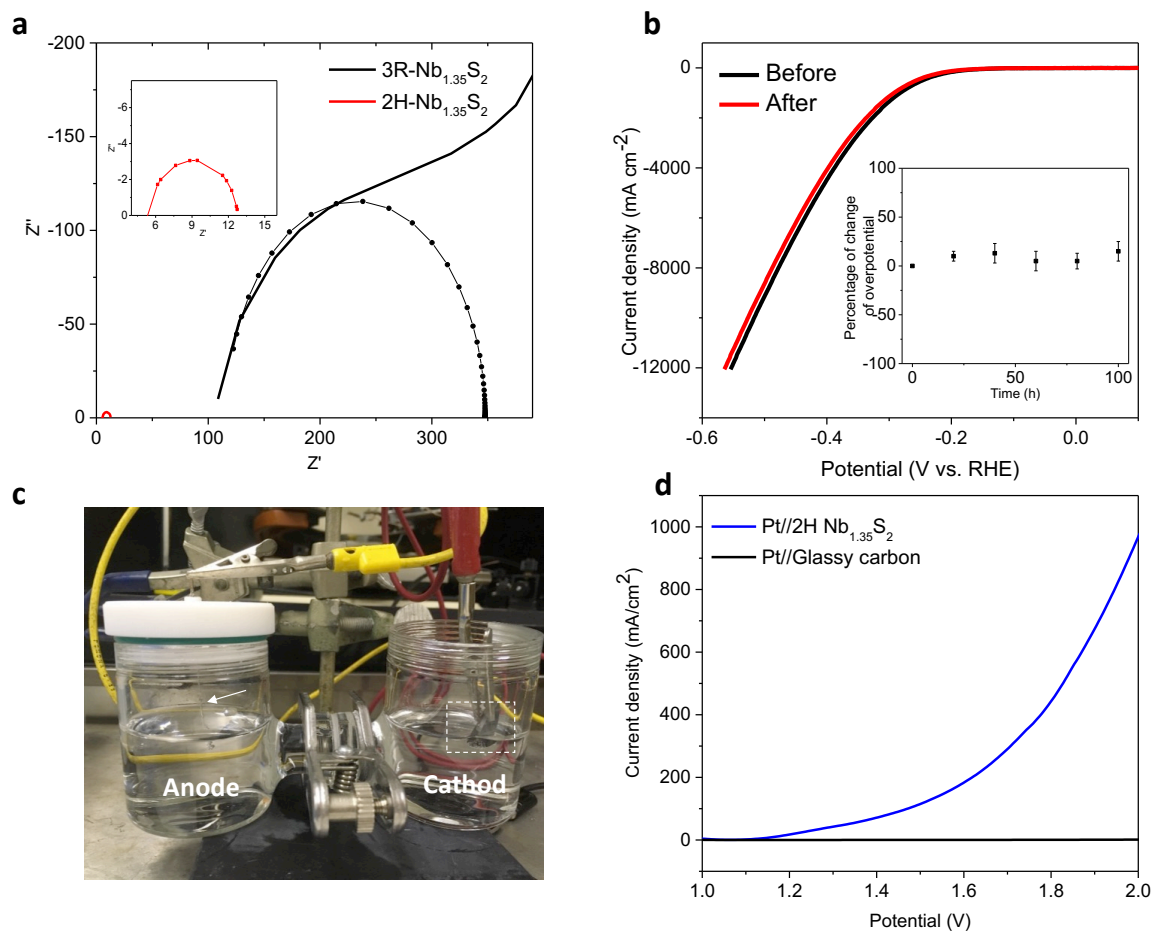
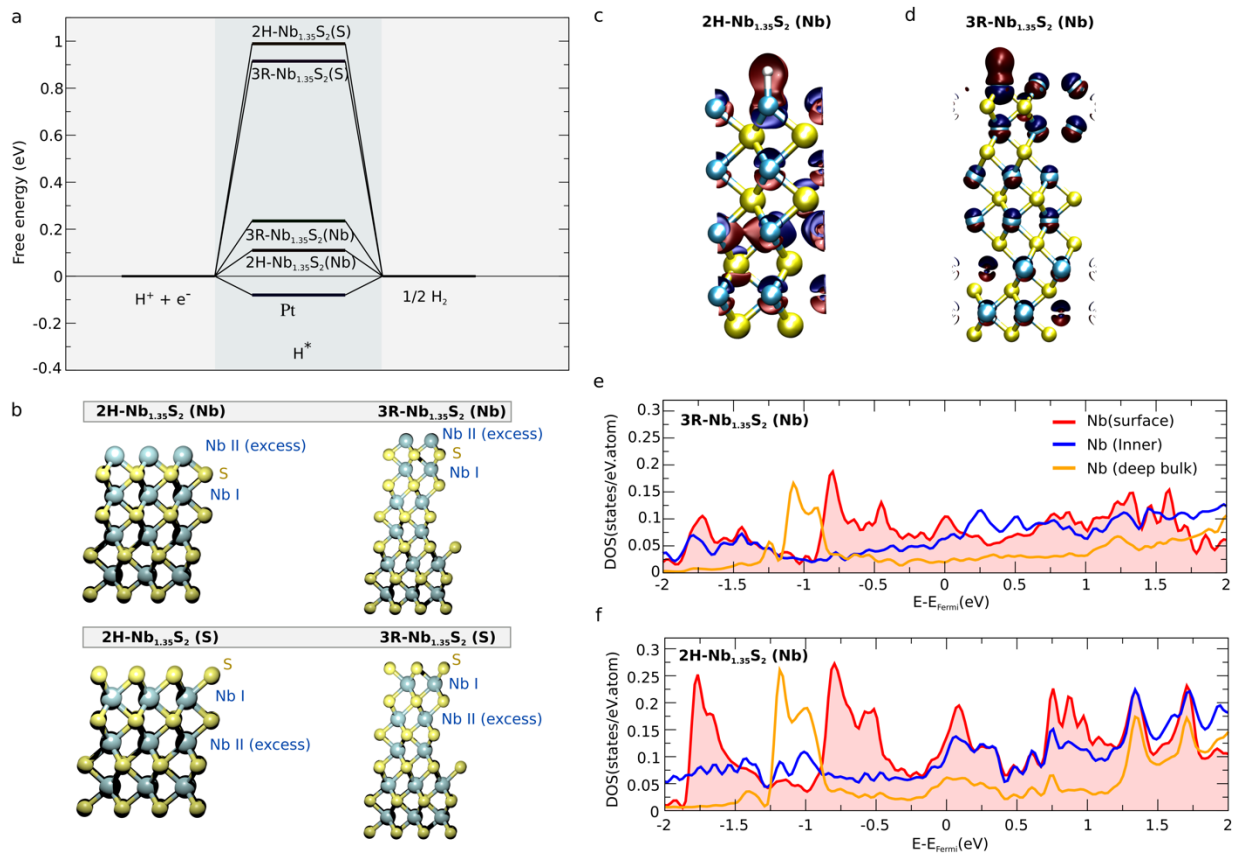


Figure 4



References

1. Lukowski, M. A. *et al.* Enhanced Hydrogen Evolution Catalysis from Chemically Exfoliated Metallic MoS<sub>2</sub> Nanosheets. *J. Am. Chem. Soc.* **135**, 10274–10277 (2013).
2. Voiry, D. *et al.* Conducting MoS<sub>2</sub> Nanosheets as Catalysts for Hydrogen Evolution Reaction. *Nano Lett.* **13**, 6222–6227 (2013).
3. Voiry, D. *et al.* Enhanced catalytic activity in strained chemically exfoliated WS<sub>2</sub> nanosheets for hydrogen evolution. *Nat. Mater.* **12**, 850 (2013).
4. Liu, Y. *et al.* Self-optimizing, highly surface-active layered metal dichalcogenide catalysts for hydrogen evolution. *Nat. Energy* **2**, 17127 (2017).
5. Shi, J. *et al.* Two-dimensional metallic tantalum disulfide as a hydrogen evolution catalyst. *Nat. Commun.* **8**, 958 (2017).
6. Li, H. *et al.* Atomic-Sized Pores Enhanced Electrocatalysis of TaS<sub>2</sub> Nanosheets for Hydrogen Evolution. *Adv. Mater.* **28**, 8945–8949 (2016).
7. Yuan, J. *et al.* Facile Synthesis of Single Crystal Vanadium Disulfide Nanosheets by Chemical Vapor Deposition for Efficient Hydrogen Evolution Reaction. *Adv. Mater.* **27**, 5605–5609 (2015).
8. Chia, X., Ambrosi, A., Lazar, P., Sofer, Z. & Pumera, M. Electrocatalysis of layered Group 5 metallic transition metal dichalcogenides (MX<sub>2</sub>, M = V, Nb, and Ta; X = S, Se, and Te). *J. Mater. Chem. A* **4**, 14241–14253 (2016).
9. Jaramillo, T. F. *et al.* Identification of Active Edge Sites for Electrochemical H<sub>2</sub> Evolution from MoS<sub>2</sub> Nanocatalysts. *Science* **317**, 100–102 (2007).
10. Zhigang, S., Baolian, Y. & Ming, H. Bifunctional electrodes with a thin catalyst layer for 'unitized' proton exchange membrane regenerative fuel cell. *J. Power Sources* **79**, 82–85 (1999).

11. Altmann, S., Kaz, T. & Friedrich, K. A. Bifunctional electrodes for unitised regenerative fuel cells. *Electrochimica Acta* **56**, 4287–4293 (2011).
12. Jellinek, F., Brauer, G. & Müller, H. Molybdenum and Niobium Sulphides. *Nature* **185**, 376 (1960).
13. Merki, D. & Hu, X. Recent developments of molybdenum and tungsten sulfides as hydrogen evolution catalysts. *Energy Environ. Sci.* **4**, 3878–3888 (2011).
14. Benck, J. D., Hellstern, T. R., Kibsgaard, J., Chakthranont, P. & Jaramillo, T. F. Catalyzing the Hydrogen Evolution Reaction (HER) with Molybdenum Sulfide Nanomaterials. *ACS Catal.* **4**, 3957–3971 (2014).
15. Voiry, D. *et al.* The role of electronic coupling between substrate and 2D MoS<sub>2</sub> nanosheets in electrocatalytic production of hydrogen. *Nat. Mater.* **15**, 1003 (2016).
16. Yin, Y. *et al.* Contributions of Phase, Sulfur Vacancies, and Edges to the Hydrogen Evolution Reaction Catalytic Activity of Porous Molybdenum Disulfide Nanosheets. *J. Am. Chem. Soc.* **138**, 7965–7972 (2016).
17. Kibsgaard, J., Chen, Z., Reinecke, B. N. & Jaramillo, T. F. Engineering the surface structure of MoS<sub>2</sub> to preferentially expose active edge sites for electrocatalysis. *Nat. Mater.* **11**, 963 (2012).
18. Kong, D. *et al.* Synthesis of MoS<sub>2</sub> and MoSe<sub>2</sub> Films with Vertically Aligned Layers. *Nano Lett.* **13**, 1341–1347 (2013).
19. Tsai, C., Abild-Pedersen, F. & Nørskov, J. K. Tuning the MoS<sub>2</sub> Edge-Site Activity for Hydrogen Evolution via Support Interactions. *Nano Lett.* **14**, 1381–1387 (2014).
20. Eda, G. *et al.* Photoluminescence from Chemically Exfoliated MoS<sub>2</sub>. *Nano Lett.* **11**, 5111–5116 (2011).



21. Pan, H. Metal Dichalcogenides Monolayers: Novel Catalysts for Electrochemical Hydrogen Production. *Sci. Rep.* **4**, 5348 (2014).
22. Tsai, C., Chan, K., Nørskov, J. K. & Abild-Pedersen, F. Theoretical insights into the hydrogen evolution activity of layered transition metal dichalcogenides. *Surf. Sci.* **640**, 133–140 (2015).
23. Yu, Y. *et al.* Layer-Dependent Electrocatalysis of MoS<sub>2</sub> for Hydrogen Evolution. *Nano Lett.* **14**, 553–558 (2014).
24. Han, N. *et al.* Nitrogen-doped tungsten carbide nanoarray as an efficient bifunctional electrocatalyst for water splitting in acid. *Nat. Commun.* **9**, 924 (2018).
25. Kibsgaard, J., Jaramillo, T. F. & Besenbacher, F. Building an appropriate active-site motif into a hydrogen-evolution catalyst with thiomolybdate [Mo<sub>3</sub>S<sub>13</sub>]<sup>2-</sup> clusters. *Nat. Chem.* **6**, 248 (2014).
26. Xie, J. *et al.* Defect-Rich MoS<sub>2</sub> Ultrathin Nanosheets with Additional Active Edge Sites for Enhanced Electrocatalytic Hydrogen Evolution. *Adv. Mater.* **25**, 5807–5813 (2013).
27. Li, H. *et al.* Activating and optimizing MoS<sub>2</sub> basal planes for hydrogen evolution through the formation of strained sulphur vacancies. *Nat. Mater.* **15**, 48 (2016).

**Acknowledgments:** MC, JY acknowledge financial support from AFOSR FA9550-16-1-0289. MC, YW acknowledge support from NSF ECCS-1608389. MC and XS acknowledge support from Shenzhen Peacock Plan (Grant No. KQTD2016053112042971). MC and ARM acknowledge financial support from the Ministry of Higher Education Malaysia. HYJ acknowledges the support from Creative Materials Discovery Program through the National Research Foundation of Korea (NRF-2016M3D1A1900035). E.J.G.S. acknowledges the use of

computational resources from the UK national high-performance computing service (ARCHER) for which access was obtained via the UKCP consortium (EPSRC grant ref EP/K013564/1); the UK Materials and Molecular Modelling Hub for access to THOMAS supercluster, which is partially funded by EPSRC (EP/P020194/1). The Queen's Fellow Award through the grant number M8407MPH, the Enabling Fund (A5047TSL), and the Department for the Economy (USI 097) are also acknowledged.

### **Author Contributions**

MC conceived the idea and supervised the project. JY and ARM designed the experiments with guidance from MC. JY performed the electrochemical measurements and analyses with advice from RF and DV. ARM synthesized the  $\text{Nb}_{1.35}\text{S}_2$  samples and characterized them. YW made the devices for HER measurements and made electrical measurements. XS and IB made  $\text{NbS}_2$  samples and characterized them with the help of FZ. HYJ prepared the FIB samples, performed the STEM analyses on the samples. MA and EJGS provided theoretical insight for the experimental results. MC, HYJ, JY, DV, RF and HS analyzed the data. MC wrote the paper with JY and all of the authors edited the manuscript before submission.

### **Methods**

**Growth of 2H- $\text{Nb}_{1+x}\text{S}_2$  and 3R- $\text{Nb}_{1+x}\text{S}_2$ :**  $\text{Nb}_{1+x}\text{S}_2$  growth was achieved under low pressure in a horizontal furnace (Lindberg/Blue M) with 1-inch diameter quartz tube. Two small quartz tubes (diameter  $\sim 9\text{mm}$ ) loaded with niobium chloride ( $\text{NbCl}_5$ , Alfa Aesar, 99.9%) and sulfur powder (Alfa Aesar, 99.5%), were placed upstream of the furnace as shown in Extended Data Fig. 6. The substrates ( $\text{SiO}_2/\text{Si}$  and glassy carbon) were placed face up above an alumina boat in the center

zone of the furnace. The tube was initially pumped to a base pressure of 20 Torr for 30min. The furnace was heated up to 850 °C with a ramp rate of 55 °C/min with a flow of 90 sccm Ar. Then, the furnace was heated up to 1000 °C with a ramp rate of 6 °C/min under a flow of 90 sccm H<sub>2</sub>/Ar (10% H<sub>2</sub> in Ar). The NbCl<sub>5</sub> was sublimated via a heating belt at 260~300 °C within 5min when the furnace reached to 1000 °C as indicated by the heating cycle shown in Extended Data Fig. 7. After growth for 8 min at 1000 °C, the whole system was naturally cooled down to room temperature.

**Synthesis of 2H-NbS<sub>2</sub>:** 2H-NbS<sub>2</sub> was synthesized by CVD using niobium oxide (Nb<sub>2</sub>O<sub>5</sub>, 99.9% Sigma-Aldrich) mixed with alkali halide (potassium iodine, KI) and sulfur powder (99.5%, Alfa Aesar). Since niobium oxide has a high melting point, alkali halide is used to create a new eutectic point for the reaction to produce more volatile oxides.<sup>28</sup> The mixture of 150 mg of Nb<sub>2</sub>O<sub>5</sub> and 100 mg of KI powders in alumina boat was loaded at the center of the tube furnace and SiO<sub>2</sub> substrates were placed above the powder with its polished side facing down. 100 mg of S powder was loaded in the upstream region of the tube. Then, 80 sccm carrier gas (10 % of H<sub>2</sub> in Ar) was introduced for 20 min to remove oxygen in the furnace. The furnace was heated with a ramp rate of 33 °C/min to the growth temperatures (1000 °C) and held at 1000 °C for 30 min before cooling down. The upstream region reached 200 °C during the growth. The thin 2H NbS<sub>2</sub> crystals and their corresponding Raman spectrum are shown in Extended Data Fig. 8a,b.

**Synthesis of 3R-NbS<sub>2</sub>:** 3R-NbS<sub>2</sub> crystals were grown by a chemical vapor transport (CVT) method which has been employed to prepare other layered compounds.<sup>29</sup> Prior to crystal growth, a quartz tube containing high purity source (Nb 99.99% and S 99.99% with a molar ratio of Nb:S is 1:2) was evacuated at 10<sup>-6</sup> Torr and sealed. The sealed quartz tube was then inserted into the tube furnace. The furnace was heated up to 900 °C with a ramp rate of 3°C/min. The reaction time was 18 h at 900 °C and the furnace was cooled down naturally. The CVT grown 3R crystals and the corresponding Raman spectrum are shown in Extended Data Fig. 8c,d.

**Electrochemical measurements:** Electrochemical measurements were performed in a three-electrode cell using a Versa Stat 3 potentiostat from Princeton Applied research. All measurements were made in 0.5 M H<sub>2</sub>SO<sub>4</sub> electrolyte purged with Ar gas. A saturated calomel electrode (Pine Instrument) and glassy carbon were used as the reference electrode and counter electrode,

respectively. Extended Data Fig. 9 shows the polarization curves obtained from 2H Nb<sub>1.35</sub>S<sub>2</sub> using platinum and carbon counter electrode. No noticeable difference was observed, and this excludes any Pt contamination during the measurements. The glassy carbon plate (Ted pella) loaded with 3R- and 2H-Nb<sub>1.35</sub>S<sub>2</sub> was used as a working electrode. 3R-NbS<sub>2</sub> was dispersed into toluene and sonicated for 1h. The solution was deposited onto glassy carbon electrode (0.1 mg/cm<sup>2</sup>) and dried. 1T-MoS<sub>2</sub> was prepared by the exfoliation of 2H-MoS<sub>2</sub> by n-BuLi following literature.<sup>20</sup> 1T-MoS<sub>2</sub> solution was loaded onto glassy carbon electrode (4 μg/cm<sup>2</sup>) and 2H-MoS<sub>2</sub> powder is dispersed into the mixed solution with DI water/IPA (the volume ratio 4:1) and sonicated for 1h to drop onto the glassy carbon electrode. All polarization curves were measured at the scan rate of 5 mVs<sup>-1</sup>. All potentials are referenced to RHE. In 0.5 M H<sub>2</sub>SO<sub>4</sub>, E(RHE)=E(SCE) + 0.254 V. Impedance measurements were performed at -0.22 V versus RHE from 1MHz to 0.1 Hz with a 5 mV a.c. amplitude.

**Device fabrication of 2H-NbS<sub>2</sub>:** To demonstrate the HER performance of 2H-NbS<sub>2</sub>, we carried out HER test using an electrochemical microcell.<sup>15</sup> We performed e-beam lithography to put gold contacts on as-grown 2H-NbS<sub>2</sub> on SiO<sub>2</sub> (300 nm) substrate. The gold electrodes were deposited via e-beam evaporation under high vacuum conditions (10<sup>-7</sup> Torr). After this process, we performed another e-beam lithography step to open a window on 2H-NbS<sub>2</sub> and cover the gold electrodes to avoid contact with electrolyte. The device is shown in Extended Data Fig. 10. Electrochemical measurements were performed in 0.5 M H<sub>2</sub>SO<sub>4</sub> and glassy carbon and Ag/AgCl electrodes were used as counter and reference electrodes, respectively.

**Electrochemical surface area measurements:** The estimation of electrochemically active surface area was conducted by measurement of the double-layer capacitance in a potential region with no faradaic response. Cyclic voltammetric (CV) measurements were performed between 285 mV and 315 mV vs. RHE at various scan rates from 5 mVs<sup>-1</sup> to 100 mVs<sup>-1</sup> in order to estimate the double layer capacitance (C<sub>dl</sub>), see Extended Data Fig. 5. Roughness factor (RF) was estimated from the ratio of the measured double layer capacitance with respect to the specific capacitance of glassy carbon electrode (0.87 mF/cm<sup>2</sup>). Our image analysis of the electrode surface (Extended Data Fig. 4) shows that only ~ 20% of the glassy carbon electrode is covered by the catalyst.

Therefore, to calculate the RF, we take the areal capacitance of the glassy carbon after catalyst deposition to be  $(0.87 \text{ mF}\cdot\text{cm}^{-2})(0.8) = 0.7 \text{ mF}\cdot\text{cm}^{-2}$ . Thus, the RF is given by:

$$\text{RF} = \frac{9.6 \text{ mF cm}^{-2}}{0.7 \text{ mF cm}^{-2}} = 13.7$$

**Turnover frequency calculation:** According to previous literature, turnover frequency can be obtained following equation.

$$\text{TOF (s}^{-1}\text{)} = \frac{J \left(\frac{\text{A}}{\text{cm}^2}\right)}{n \times N \times \text{RF} \times (1.602 \times 10^{-19} \text{C})}$$

To determine the density of active sites ( $N$ ), we assume the lattice constant of  $2\text{H-Nb}_{1.35}\text{S}_2$  is  $3.31 \text{ \AA}$  (Figure 1c, STEM image).  $n$  is the number of electrons involved in the reaction. The surface area of unit cell can be  $9.4 \times 10^{-16} \text{ cm}^2$ . We assumed that entire basal plane can be catalytically active. Therefore, the density of active is estimated to be about  $1.06 \times 10^{15} \text{ cm}^{-2}$ . The density of the surface active sites of  $2\text{H Nb}_{1.35}\text{S}_2$  on geometric area :  $1.06 \times 10^{15} \text{ sites/cm}^2 \times 13.7 = 1.4 \times 10^{16} \text{ sites/cm}^2$

To get TOF at exchange current density, the exchange current density was extrapolated linearly from the Tafel slope. The exchange current density of  $2\text{H-Nb}_{1.35}\text{S}_2$  is  $800 \mu\text{A/cm}^2$  which is remarkable value among the reported TMD based catalysts as listed in Extended Data Table 1.

**Electrical conductivity measurements:** The conductivity of the intercalated phases was measured and by evaporating gold contacts and is shown in Extended Data Fig. 11. We find the  $2\text{H Nb}_{1.35}\text{S}_2$  phase to be highly conducting compared to other reports in the literature.<sup>30-33</sup>

**Computational Methods:** The calculations were done using the plane wave density functional theory (DFT) Vienna ab-initio simulation package (VASP)<sup>34-37</sup> The van der Waals interactions were taken into account at the level of opt-B88 functional<sup>38</sup> and the Bayesian error estimation exchange-correlation functional with long-range interactions<sup>39</sup> (BEEF-vdW). A 500 eV plane-wave cutoff was used, and the Brillouin zone was sampled with a Monkhorst-Pack<sup>40</sup> sampling of  $3 \times 3 \times 1$  k-points grid for the relaxation and a  $15 \times 15 \times 1$  k-points for the energy calculations. The  $\Delta G_{\text{H}}$  were calculated using the formula:

$$\Delta G_H = \Delta E + \Delta(ZPE) - T\Delta S$$

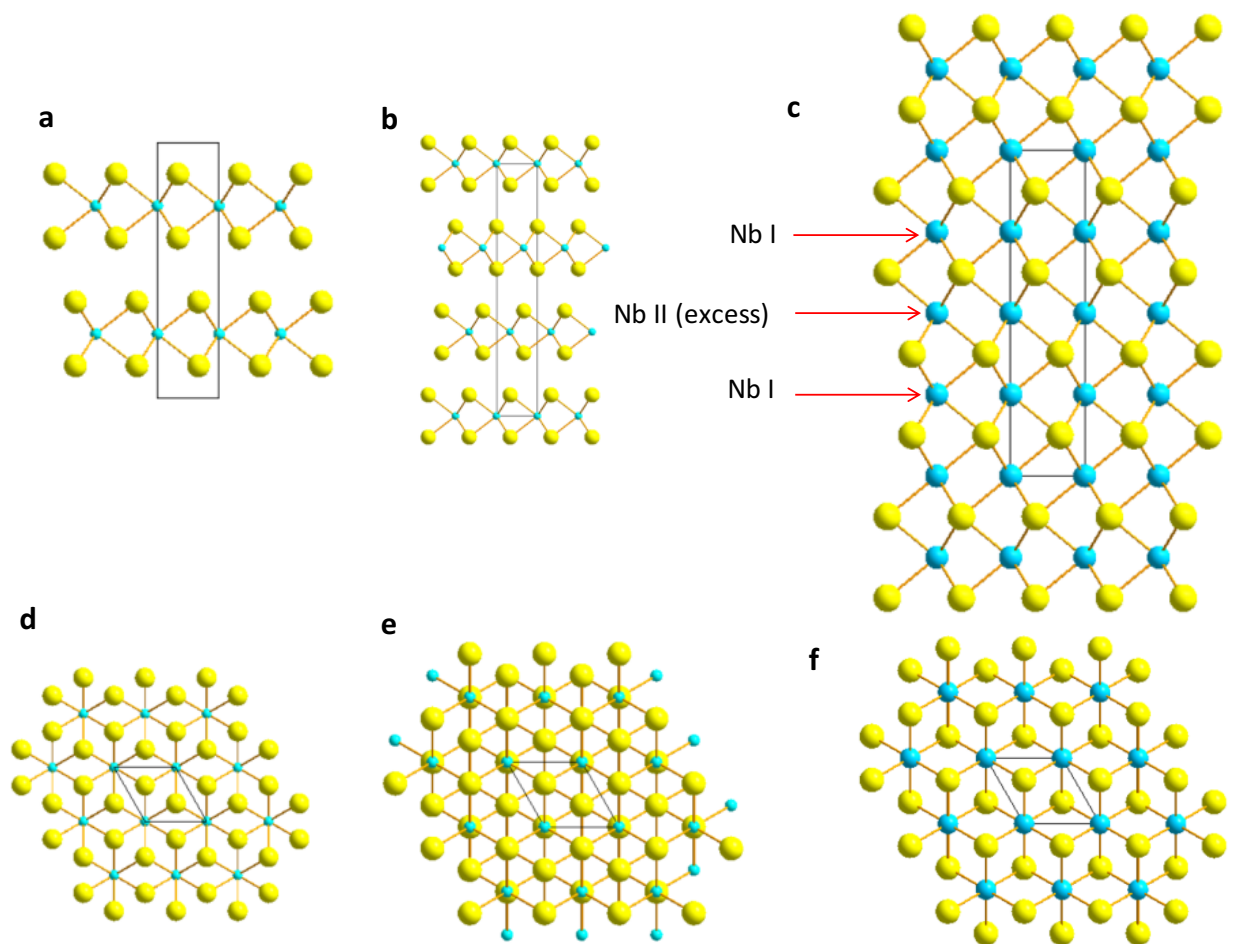
with

$$\Delta E = E(\text{surface} + H) - E(\text{surface}) - \frac{1}{2}E(H_2)$$

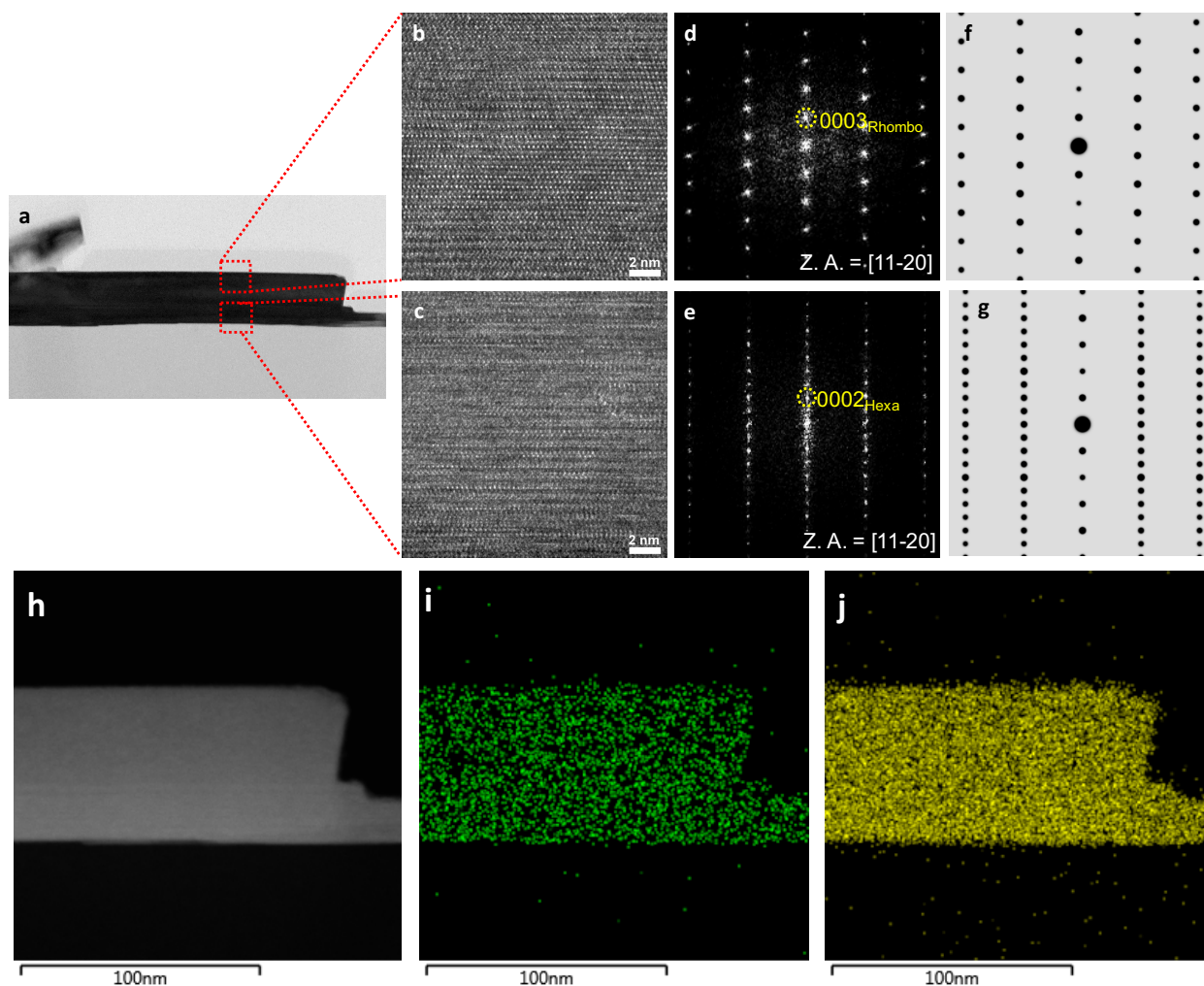
$$\Delta(ZPE) = ZPE_H - \frac{1}{2}ZPE_{H_2}$$

$$T\Delta S = \frac{-1}{2}TS_{H_2} = -0.205eV$$

Where  $E(\text{surface} + H)$  is the total energy of the system with the H-atom bound at the basal plane,  $E(\text{surface})$  is the total energy of the pristine system,  $E(H_2)$  is the total energy of the  $H_2$  molecule.  $\Delta(ZPE)$  is the difference between the zero-point energy (ZPE) of the H-atom and the zero-point energy of the  $H_2$  molecule, calculated using the normal mode analysis. We will use the entropy of the molecular hydrogen in the gas phase at standard conditions (1 bar of  $H_2$ , pH=0 and T=300 K). The bulk lattice parameters calculated using ab initio opt B88-vdW and BEEF-vdW functionals are shown in Extended Data Tables 3 and 5, as well their energetics as displayed in Extended Tables 4, 6, 7 and 8. The corresponding crystal structures obtained from these parameters are shown in Extended Data Figure 12.

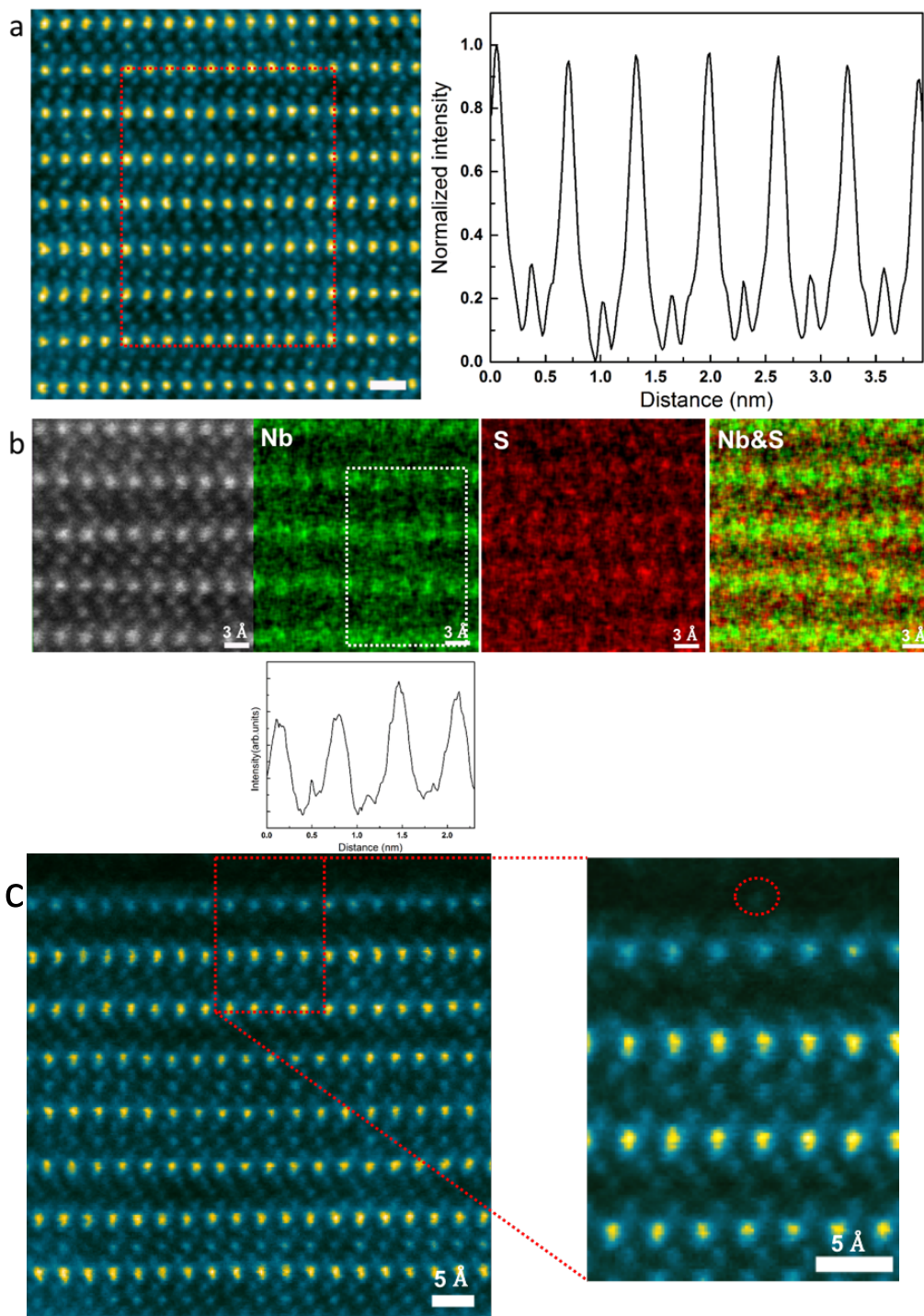


**Extended Data Fig. 1 | Phases of NbS<sub>2</sub>.** (a, b) Side view and (d, e) top view of 2H hexagonal (P63/mmc symmetry) and 3R rhombohedral (R3m symmetry) phases of NbS<sub>2</sub>. (c, f) Side and top views of 2H phase Nb<sub>1.35</sub>S<sub>2</sub> phase. The excess of Nb (labelled as Nb II in the c) occupies octahedral configuration while the Nb I are in trigonal prismatic sites. The Nb<sub>1.35</sub>S<sub>2</sub> phase can also occur in the 3R phase.



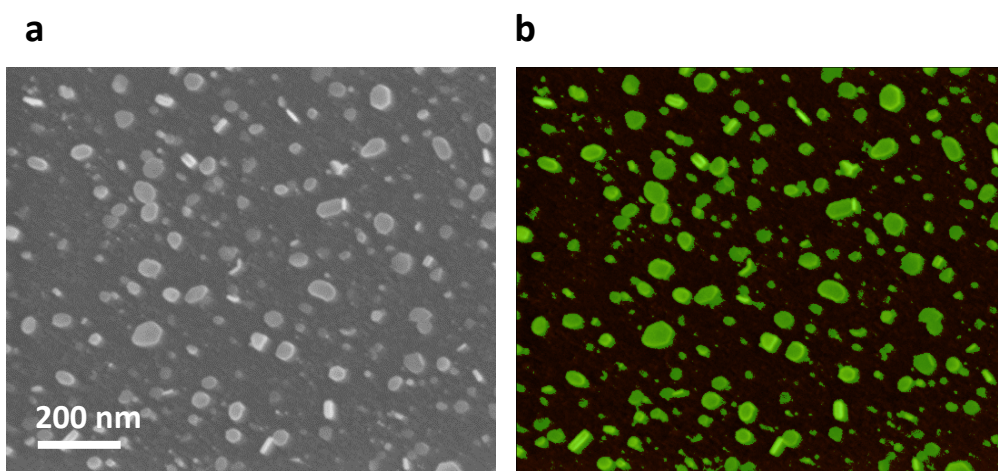
**Extended Data Fig. 2 | TEM of  $\text{Nb}_{1.35}\text{S}_2$  and corresponding diffraction images.** **a**, Low magnification BFTEM image of cross-sectional FIB sample (thickness = 40 nm) prepared from CVD grown samples on  $\text{SiO}_2$ . **b**, **c** HRTEM images taken from top of the sample and bottom of the sample as indicated by square dotted regions on the left image. **d**, **e** Fast Fourier transform (FFT) pattern indicating that the top (thicker) region is rhombohedral while the bottom (thin) region is in hexagonal configuration based on their very good agreement with simulated patterns shown in **f** (simulated ED patterns for intercalated 3R phase) and **g** (simulated ED for intercalated 2H phase). **h**, Low magnification of image of the FIB cross section and the corresponding Energy Dispersive Spectroscopy map showing Nb (**i**) and S (**j**) in the sample.



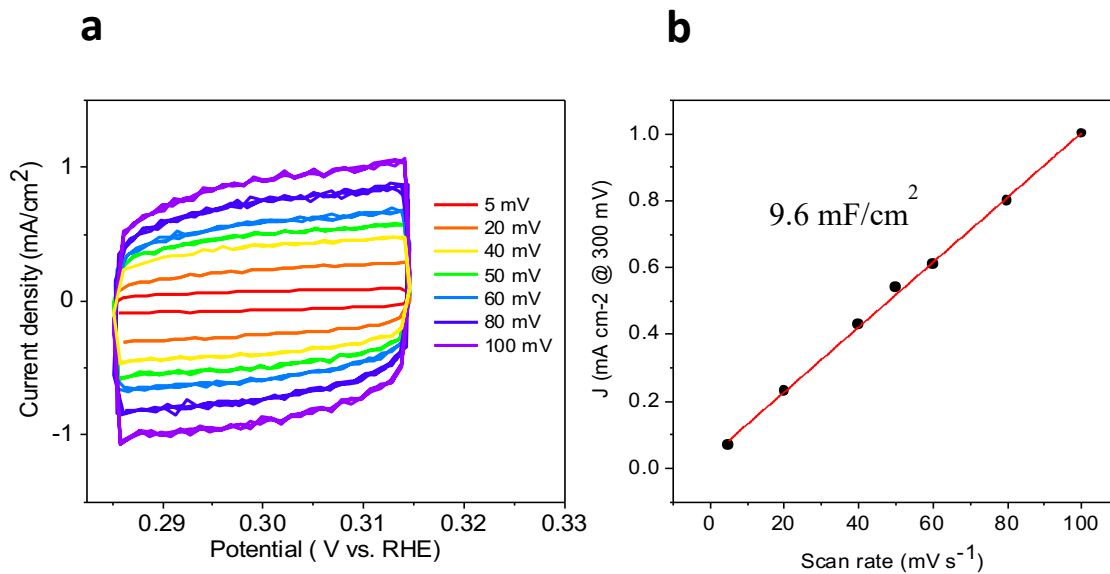


**Extended Data Fig. 3 | Line scan and chemical analyses in STEM.** **a**, Annular dark field image (left) and the corresponding (right) intensity line scan of 2H Nb<sub>1.35</sub>S<sub>2</sub> phase showing that Nb atoms are present between the layers. **b**, Black and white unfiltered STEM image and corresponding elemental maps of Nb, S, and both Nb and S obtained using energy dispersive x-ray spectroscopy. The mapping and the line scan below the Nb map confirm that the intercalated atoms are Nb. **c**,

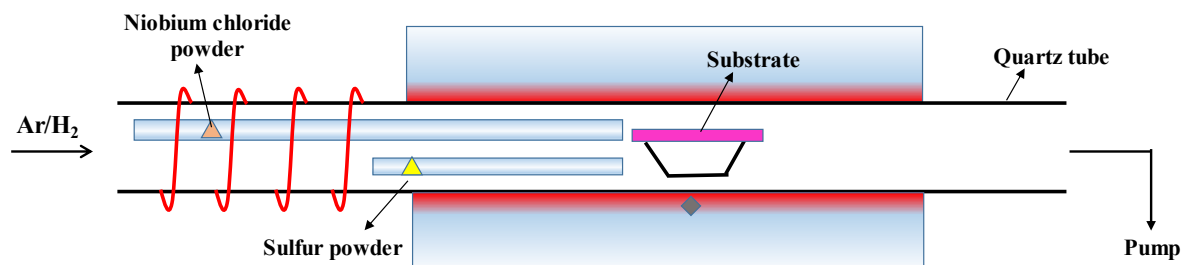
STEM image of 2H phase  $\text{Nb}_{1.35}\text{S}_2$  with an enlargement of the surface region shown on the right. Faint images of Nb atoms terminating the surface can be observed as indicated by the dotted red circle.



**Extended Data Fig. 4 | Image analyses of areal coverage of catalysts on electrode surface. a,** SEM image of 2H- $\text{Nb}_{1.35}\text{S}_2$ . **b,** Image analyses was used to highlight (in green) the  $\text{Nb}_{1.35}\text{S}_2$  flakes on the glassy carbon electrode (black background). Then the percent of area covered by the flakes was calculated. A total of 15 images were taken and the average area covered by the catalyst  $\text{Nb}_{1.35}\text{S}_2$  flakes was approximately  $20\% \pm 3\%$  of the electrode surface.

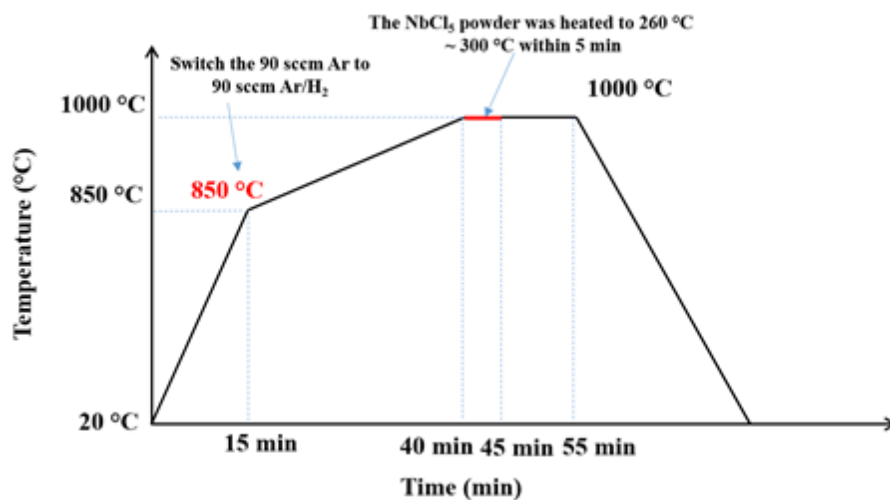


**Extended Data Fig. 5 | Electrochemical surface area measurements. a**, CV curves of Nb<sub>1.35</sub>S<sub>2</sub> electrodes measured between 285 and 315 mV vs. RHE. **b**, Current density at 300 mV plotted against cyclic voltammetry scan rate.

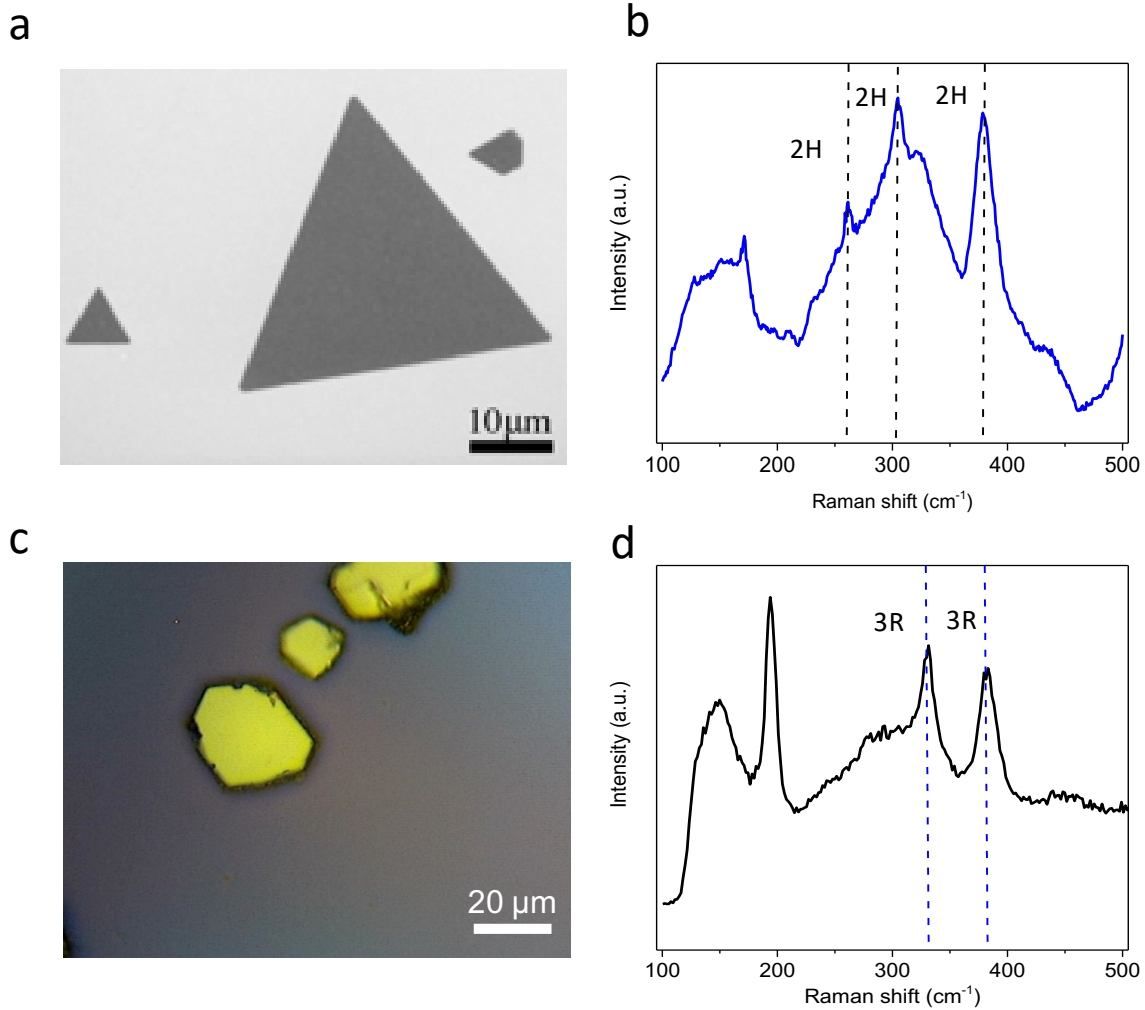


**Extended Data Fig. 6 | Schematic of chemical vapor deposition setup for  $\text{Nb}_{1+x}\text{S}_2$  synthesis.**

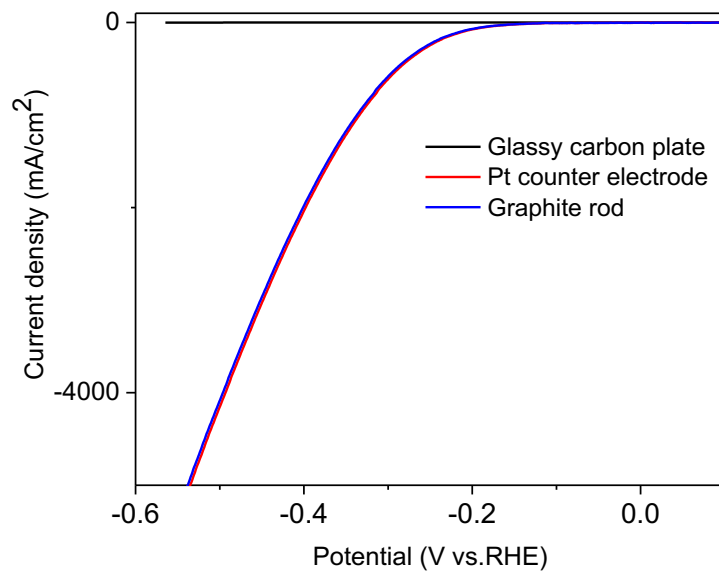
The precursors are placed upstream because they sublime at a much lower temperature than the growth temperature.



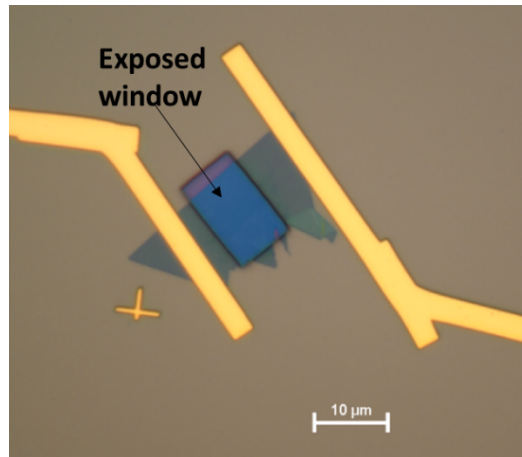
**Extended Data Fig. 7 | Heating ramp and cooling cycle growth of  $\text{Nb}_{1+x}\text{S}_2$ .** The tube furnace was initially heated in Ar atmosphere, then in reducing atmosphere and growth was conducted for 10 – 20 minutes to achieve different thicknesses.



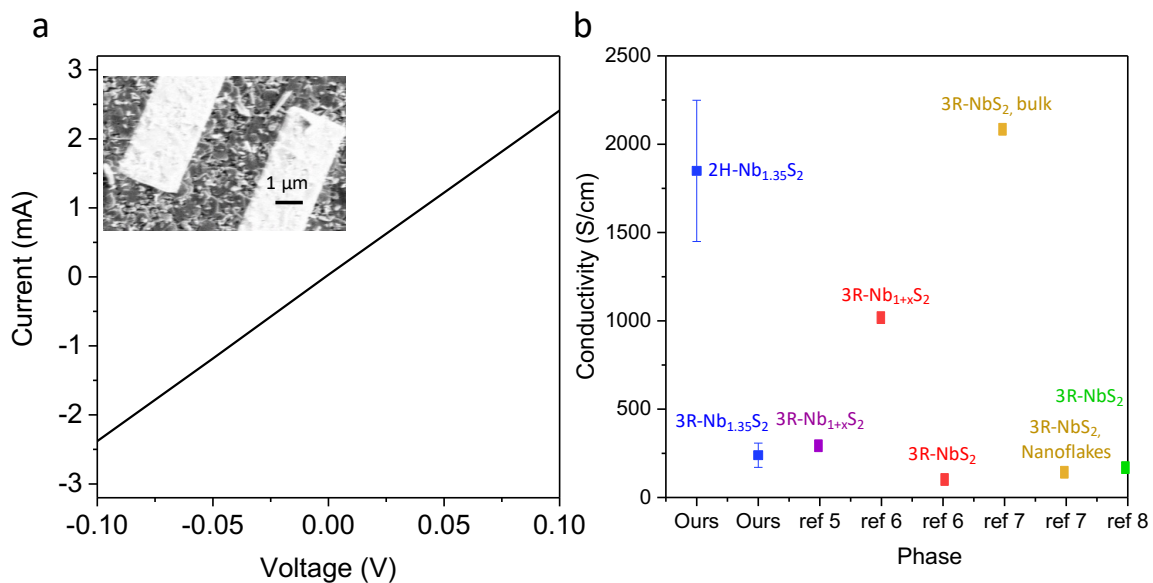
**Extended Data Fig. 8 | Different phases of NbS<sub>2</sub>.** **a**, SEM image of CVD grown 2H-NbS<sub>2</sub> with lateral dimensions of 5-20 μm and **b**, Raman spectrum of 2H-NbS<sub>2</sub> shows peaks at 260, 304 and 379 cm<sup>-1</sup>. **c**, Optical microscope image of 3R-NbS<sub>2</sub> grown by CVT and **d**, Raman spectrum of 3R-NbS<sub>2</sub> shows E<sub>2g</sub> and A<sub>1g</sub> peaks at 330 cm<sup>-1</sup> and 385 cm<sup>-1</sup>, respectively.



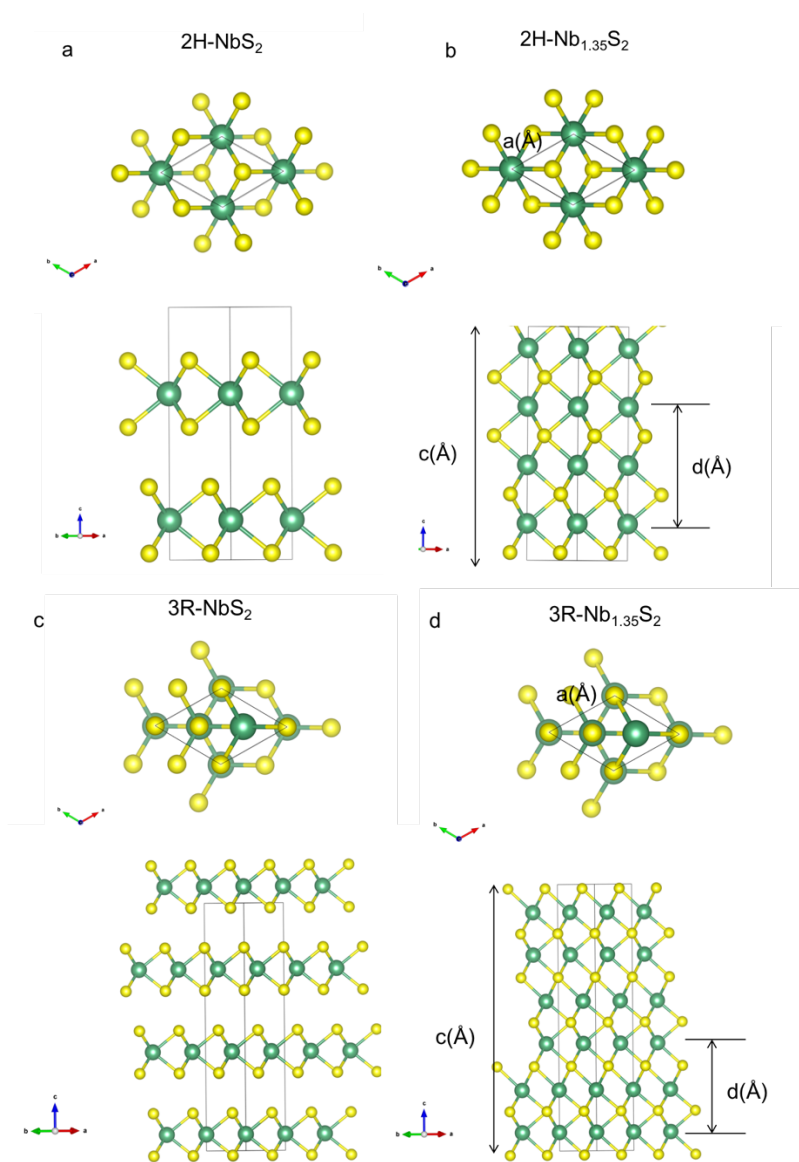
**Extended data Fig. 9** | Pt vs glassy carbon as counter electrode. Polarization curves for glassy carbon plate and  $2\text{H Nb}_{1.35}\text{S}_2$  using Pt or carbon as counter electrode.



**Extended data Fig. 10 | Electrochemical microcell devices.** Optical image of an electrochemical microcell with 2H-NbS<sub>2</sub> as the catalyst. The blue region is the NbS<sub>2</sub> flake and rectangular gold contacts are patterned onto it. A window is opened lithographically so that catalysis measurements can be made. The entire area is covered by PMMA except the window so the electrolyte can only interact with the catalyst.

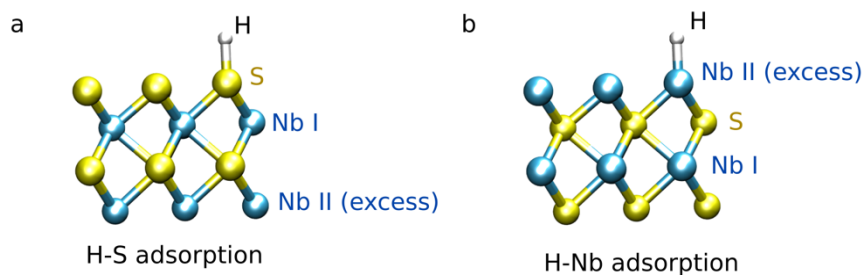


**Extended data Fig. 11 | Electrical properties of different NbS<sub>2</sub>.** **a**, I-V curve measured for the 2H Nb<sub>1.35</sub>S<sub>2</sub> nanoflakes. The inset shows a SEM image of the device. An average value of 1800 S/cm was obtained with the highest value being > 2400 S/cm. **b**, Comparison of conductivities for NbS<sub>2</sub>. NbS<sub>2</sub> is known as a metallic TMD material. However, the conductivity values in literature are scattered.<sup>30-33</sup>



**Extended data Fig. 12** | Definition of geometrical parameters used at Extended Data Table 3 at regular 2H-NbS<sub>2</sub> and 3R-NbS<sub>2</sub> phases as well as in the intercalated 2H-Nb<sub>1.35</sub>S<sub>2</sub>, 3R-Nb<sub>1.35</sub>S<sub>2</sub> phases.





**Extended data Fig. 13** | Definition of the geometry utilized to calculate the energetics of H at a monolayer NbS<sub>2</sub> with an additional Nb layer into the system. This would correspond to the smallest “intercalated phase” before it established in a 2H or 3R phases. The energetics for these systems are shown in Extended Data Table 7.

**Extended Data Table 1** | Comparison of TOF and exchange current density of TMDs catalysts

	$J_0$ ( $\mu A/cm^2$ )	TOF at $J_0$	ref
2H-Nb <sub>1.35</sub> S <sub>2</sub>	800 ± 100	0.17s <sup>-1</sup> ± 0.03	Our work
2H-MoS <sub>2</sub> /Au	7.9	-	9
1T-WS <sub>2</sub>	20	0.043	3
2H-TaS <sub>2</sub>	100-179.47	-	5
Pt	450	0.9	9

**Extended Data Table 2** | Parameters used for synthesis of Nb<sub>1+x</sub>S<sub>2</sub>

	NbCl <sub>5</sub>	S	Temperature of NbCl <sub>5</sub>
3R-Nb <sub>1+x</sub> S <sub>2</sub>	35 mg	200 mg	300 °C
2H-Nb <sub>1+x</sub> S <sub>2</sub>	20 mg	100 mg	260 °C

**Extended Data Table 3 | Bulk lattice parameters using opt-B88 functional.** Simulations of the geometrical parameters using opt-B88 functional including vdW interactions. Lattice parameter,  $a(\text{\AA})$ , interlayer distance via Nb-Nb distance,  $d(\text{\AA})$ , and supercell length,  $c(\text{\AA})$  are defined as in Extended Data Figure 12. Sound comparison with experimental data at different phases is observed.

	2H-NbS <sub>2</sub>		3R-NbS <sub>2</sub>		2H-Nb <sub>1.35</sub> S <sub>2</sub>		3R-Nb <sub>1.35</sub> S <sub>2</sub>
	Theory	Exp.	Theory	Exp.	Theory	Exp.	Theory
$a(\text{\AA})$	3.34	3.31	3.35	3.33	3.31	3.306	3.24
$d(\text{\AA})$	5.97	5.91	6.05	5.98	6.64	6.35	6.81
$c(\text{\AA})$	11.935	11.89	18.17	17.81	13.29	12.6	20.43

**Extended Data Table 4 | Thermodynamic properties of S terminated surface using opt-B88 functional.** Energetics of the intercalated phase 2H-Nb<sub>1.35</sub>S<sub>2</sub> with adsorption of H at S atoms at different coverages using opt-B88 functional. The large values of  $\Delta G_H$  (eV) at different coverages rule out any HER using S-terminate surfaces.

Coverage	2H-Nb <sub>1.35</sub> S <sub>2</sub> (H-S adsorption)		
	0.11 ML	0.25 ML	1 ML
$\Delta E$ (eV)	1.011	0.804	1.459
ZPE (eV)	0.203	0.203	0.162
$\Delta G_H$ (eV)	1.245	1.077	1.694

**Extended Data Table 5 | Bulk lattice parameters using BEEF-vdW functional.** Simulations of the geometrical parameters using BEEF-vdW functional including vdW interactions. Lattice parameter,  $a(\text{\AA})$ , interlayer distance via Nb-Nb distance,  $d(\text{\AA})$ , and supercell length,  $c(\text{\AA})$  are defined as in Extended Data Figure 12. Sound comparison with experimental data at different phases is obtained.

	2H-NbS <sub>2</sub>		3R-NbS <sub>2</sub>		2H-Nb <sub>1.35</sub> S <sub>2</sub>		3R-Nb <sub>1.35</sub> S <sub>2</sub>
	Theory	Exp.	Theory	Exp.	Theory	Exp.	Theory
$a(\text{\AA})$	3.35	3.31	3.35	3.33	3.30	3.30	3.22
$d(\text{\AA})$	6.34	5.91	6.36	5.98	6.65	6.35	6.65

c(Å)	12.67	11.89	19.10	17.81	13.30	12.6	19.94
------	-------	-------	-------	-------	-------	------	-------

**Extended Data Table 6 | Thermodynamic properties of S terminated surface using BEEF-vdW functional.** Energetics of the intercalated phases 2H-Nb<sub>1.35</sub>S<sub>2</sub> and 3R-Nb<sub>1.35</sub>S<sub>2</sub> with adsorption of H at S atoms at different coverages using BEEF-vdW functional. Similarly as in the opt-B88 functional, the S-terminated surface seems inert for HER as long as H atoms bind on S.

	2H-Nb <sub>1.35</sub> S <sub>2</sub> (H-S adsorption)			3R-Nb <sub>1.35</sub> S <sub>2</sub> (H-S adsorption)
Coverage	0.11 ML	0.25 ML	1 ML	0.25 ML
ΔE (eV)	1.005	0.766	1.41	0.619
ZPE (eV)	0.226	0.226	0.16	0.226
ΔG <sub>H</sub> (eV)	1.302	0.989	1.64	0.915

**Extended Data Table 7 | Thermodynamic properties of a monolayer NbS<sub>2</sub> with additional Nb atoms in the structure.** Energetics of the monolayer NbS<sub>2</sub> with additional Nb atoms incorporated into the structure (see Extended Data Fig. 13). This system corresponds to the smallest situation where the effect of additional Nb atoms could be appreciated on the free energies and HER of monolayer NbS<sub>2</sub>. The adsorption of H is simulated either at S-terminated the surface or at Nb-terminated. The large variations in energy between both configurations indicate the H adatoms would prefer binding at the Nb sites rather than on S. This suggests that additional Nb atoms have a strong effect on the chemical kinetics of the reaction changing the preferable site of H adsorption for efficient HER. Similar results as those in Ref. 22 are compared for the monolayer NbS<sub>2</sub> without additional Nb atoms. Calculations at the level of BEEF-vdW functional.

	Monolayer NbS <sub>2</sub>	Monolayer NbS <sub>2</sub> Nb terminated (H-S adsorption)	Monolayer NbS <sub>2</sub> Nb terminated (H-Nb adsorption)
Coverage	0.0625 ML	0.25 ML	0.25 ML
ΔE (eV)	-0.185	1.039	0.072
ZPE (eV)	0.226	0.215	0.098
ΔG <sub>H</sub> (eV)	0.11	1.324	0.24

**Extended Data Table 8 | Thermodynamic properties of Nb terminated slab with adsorption of H on Nb atoms.** Energetics of the intercalated phases 2H-Nb<sub>1.35</sub>S<sub>2</sub> and 3R-Nb<sub>1.35</sub>S<sub>2</sub> with adsorption of H on Nb atoms using BEEF-vdW functional. The resulting geometries are those shown in Figure 4. The comparison between 2H-Nb<sub>1.35</sub>S<sub>2</sub> and 3R-Nb<sub>1.35</sub>S<sub>2</sub> clearly indicates that the former would give better HER results than the latter, as it follows closely the measurements.

	2H-Nb <sub>1.35</sub> S <sub>2</sub> (Nb Terminated)	3R-Nb <sub>1.35</sub> S <sub>2</sub> (Nb Terminated)
Coverage	0.25 ML	0.25 ML
$\Delta E$ (eV)	-0.056	0.066
ZPE (eV)	0.099	0.098
$\Delta G_H$ (eV)	0.11	0.235

28. Li, S. *et al.* Halide-assisted atmospheric pressure growth of large WSe<sub>2</sub> and WS<sub>2</sub> monolayer crystals. *Appl. Mater. Today* **1**, 60–66 (2015).
29. Suh, J. *et al.* Doping against the Native Propensity of MoS<sub>2</sub>: Degenerate Hole Doping by Cation Substitution. *Nano Lett.* **14**, 6976–6982 (2014).
30. Huang, Y. H., Peng, C. C., Chen, R. S., Huang, Y. S. & Ho, C. H. Transport properties in semiconducting NbS<sub>2</sub> nanoflakes. *Appl. Phys. Lett.* **105**, 93106 (2014).
31. Molenda, J., Bak, T. & Marzec, J. Electrical and electrochemical properties of niobium disulphide. *Phys. Status Solidi A* **156**, 159–168 (1996).

32. Niazi, A. & Rastogi, A. K. Low-temperature resistance minimum in non-superconducting  $3R\text{-Nb}_{1+x}\text{S}_2$  and  $3R\text{-Ga}_x\text{NbS}_2$ . *J. Phys. Condens. Matter* **13**, 6787 (2001).
33. Zhao, S. *et al.* Two-dimensional metallic  $\text{NbS}_2$ : growth, optical identification and transport properties. *2D Mater.* **3**, 25027 (2016).
34. Kresse, G. & Hafner, J. Ab initio molecular dynamics for liquid metals. *Phys. Rev. B* **47**, 558–561 (1993).
35. Kresse, G. & Hafner, J. Ab initio molecular-dynamics simulation of the liquid-metal/amorphous-semiconductor transition in germanium. *Phys. Rev. B* **49**, 14251–14269 (1994).
36. Kresse, G. & Furthmüller, J. Efficiency of ab-initio total energy calculations for metals and semiconductors using a plane-wave basis set. *Comput. Mater. Sci.* **6**, 15–50 (1996).
37. Kresse, G. & Furthmüller, J. Efficient iterative schemes for ab initio total-energy calculations using a plane-wave basis set. *Phys. Rev. B* **54**, 11169–11186 (1996).
38. Klimeš, J., Bowler, D. R. & Michaelides, A. Chemical accuracy for the van der Waals density functional. *J. Phys. Condens. Matter* **22**, 22201 (2010).
39. Wellendorff, J. *et al.* Density functionals for surface science: Exchange-correlation model development with Bayesian error estimation. *Phys. Rev. B* **85**, 235149 (2012).
40. Monkhorst, H. J. & Pack, J. D. Special points for Brillouin-zone integrations. *Phys. Rev. B* **13**, 5188–5192 (1976).